

Flux-Weakening Regime Operation of an Interior Permanent-Magnet Synchronous Motor Drive

THOMAS M. JAHNS, MEMBER, IEEE

Abstract—The interior permanent magnet (IPM) synchronous motor is compatible with extended-speed-range constant-power operation by means of flux-weakening control. Flux weakening uses stator current components to counter the fixed-amplitude magnetic airgap flux generated by the rotor magnets, performing a role similar to field weakening in a separately excited dc motor. The nature of current regulator saturation caused by the finite inverter dc source voltage is described, marked by premature torque and power degradation at high speeds in the absence of flux-weakening control. This is followed by presentation of a new flux-weakening control algorithm developed as a modification of an established feedforward IPM torque control algorithm described previously in the literature. Attractive features of this new algorithm include smooth drive transitions into and out of the flux-weakening mode, fast response, as well as automatic adjustment to changes in the dc source voltage. Simulation and empirical test results from a 3-hp laboratory IPM motor drive are used to confirm the constant-power operating envelope achieved using the new flux-weakening control algorithm.

I. INTRODUCTION

A. Background

THE interior permanent-magnet (IPM) synchronous motor illustrated in Fig. 1(a) is distinguished from its more common surface permanent-magnet (SPM) counterpart (Fig. 1(b)) by the buried rotor magnets of the IPM machine. Reference [1] describes the IPM synchronous motor as a desirable candidate for adjustable-speed operation. Excited by a PWM current-regulated inverter (Fig. 2), the IPM motor drive yields attractive performance characteristics including smooth instantaneous torque, fast dynamic response, and high drive efficiency.

As a further advantage, it was noted in [1] that constant-power characteristics can be achieved over an extended speed range with the IPM motor by means of flux weakening. The term "flux weakening" is adopted in preference to the less precise "field weakening," since the rotor field of a PM motor cannot be weakened directly. Rather, the use of magnets to excite the rotor field makes it necessary to counteract the magnet-generated airgap magnetic flux at high speeds with opposing flux induced by the stator currents (familiar to some as "armature reaction" flux). Such extended-speed operating characteristics make the IPM synchronous motor a candidate for applications requiring constant-power operation such as traction and spindle drives.

Paper IPCSD 86-74, approved by the Electric Machines Committee of the IEEE Industry Applications Society for presentation at the 1986 Industry Applications Society Annual Meeting, Denver, CO, September 28–October 3. Manuscript released for publication January 22, 1987.

T. M. Jahns is with Corporate R&D, General Electric Company, Building 37, Room 380, P.O. Box 43, Schenectady, NY 12301.

IEEE Log Number 8714277.

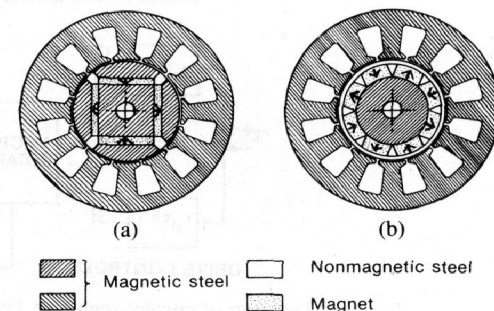


Fig. 1. Motor cross sections illustrating major features of PM synchronous motors. (a) Interior. (b) Surface.

applications for which the SPM ("brushless dc") motor drive with rectangular current excitation is not comparably well suited [2].

Flux weakening in the IPM motor drive requires special control action to carry out this weakening by appropriately adjusting the stator excitation. This is a topic which to date has received very little attention in the literature, as outlined briefly in the following section.

B. Review of Past Work

The IPM synchronous motor itself is not a new technical topic [2]–[6]. Suitability of the IPM motor for adjustable-speed operation has been addressed by only a few authors, notably Lajoie-Mazenc and his colleagues [7], [8]. The opportunities for achieving constant-power operating characteristics with an IPM drive system were recognized and developed for a traction application in [9].

In contrast, discussion to date of high-performance IPM motor drives using PWM regulation of the individual phase currents (Fig. 2) has been limited to the "constant torque" regime in which the current regulators are fully operational [1], [8]. The critical transition between normal current-regulated operation at lower speeds and flux-weakening operation poses special problems for this important class of IPM motor drives which have not been addressed previously.

C. Paper Objectives

The purpose of this paper is twofold. The first objective is to provide useful insights into the performance degradation associated with current regulator saturation in the IPM motor drive and the available improvements delivered by flux weakening. The second half of the paper presents a new control algorithm which is sensitive to current regulator saturation, providing flux-weakening operation for the IPM drive system over an extended speed range. Principal results

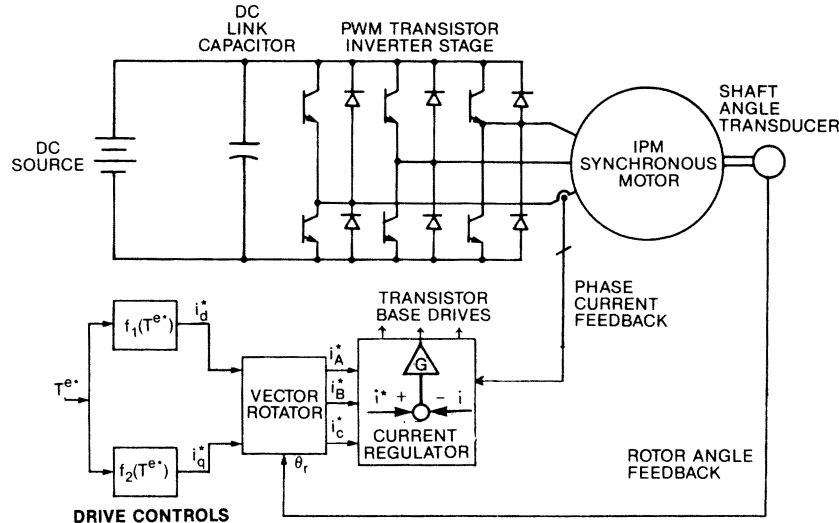


Fig. 2. Diagram of current-regulated IPM synchronous motor drive including basic feedforward torque control.

are confirmed using a combination of simulation results and empirical test data from a 3-hp laboratory IPM drive system.

II. FLUX-WEAKENING OPERATION ISSUES

A. Preliminary Motor Assumptions

The following discussion of the IPM synchronous motor is based on the familiar two-axis model of a salient-pole synchronous machine in the rotor reference frame [10] discussed in [1]. Use of this model requires adoption of a set of standard assumptions, including sinusoidal winding distribution, etc., which will not be repeated here. All of the motor model inductances are assumed to be constant parameters for simplicity.

Proposals have been made previously in the literature for modification of this basic motor model to reflect the effects of magnetic saturation [11]–[13] by such means as current-dependent inductances or by special cross-coupling elements. Magnetic saturation effects clearly demand consideration if one is attempting to accurately predict IPM motor performance for operation at lower rotor speeds. However, as discussed by Chalmers [5], the net impact of magnetic saturation on motor performance is relatively smaller at elevated speeds since higher motor reactances and back-EMF magnitudes combine to lower the peak currents. As a result, the principles described in this paper are only weakly influenced by magnetic saturation, permitting its exclusion here.

For consistency, waveforms and curves presented in several of the following figures have been generated using parameters of the laboratory 3-hp IPM motor drive described in more detail in Section IV-A.

B. Current Regulator Saturation Characteristics

An earlier paper [1] has described how smooth instantaneous torque is developed by exciting the IPM motor with balanced sinusoidal phase currents synchronized to the rotor

position. The torque amplitude is controlled by regulating the amplitudes and phase angles of the stator currents with respect to the rotor magnet orientation. As described in [1] the instantaneous phase currents can be represented in the rotor reference frame by orthogonal current components i_d and i_q , assuming d -axis alignment with the rotor magnet field. Responsive torque control is conveniently achieved by regulating the i_d and i_q components, which are both dc quantities under steady-state sinusoidal-excitation conditions.

As shown in Fig. 2, a torque command T_e^* (the asterisk indicates commanded value) is first mapped into appropriate i_d^* and i_q^* commands by functions f_1 and f_2 . These functions can be programmed to optimize some drive performance criterion, such as motor torque-per-amp, based on knowledge of the IPM motor parameters [1]. These rotor-referred current commands i_d^* and i_q^* (see Fig. 2) are then transformed to the corresponding phase current commands i_A^* , i_B^* , and i_C^* in the stationary frame using rotor angle feedback information.

Closed-loop current regulators are responsible for controlling the applied PWM voltage excitation so that the instantaneous phase currents follow their commanded values within narrow limits determined by the regulator gains. Tight regulation of the stator phase currents forces the stator current components i_d and i_q in the rotor reference frame to likewise closely match their commanded values i_d^* and i_q^* . The stator current regulators might adopt one of many alternate implementations such as the familiar hysteresis or ramp-comparison configurations [14].

Saturation of the current regulators occurs at elevated speeds when the motor terminal voltage increases sufficiently to approach the maximum voltage that the drive inverter can apply. Rotor speed is an important factor, determining the onset of regulator saturation, since the motor reactances and back-EMF are all proportional to the excitation frequency, which is permanently synchronized with the rotor speed. By setting the motor terminal voltage at its maximum value available from the dc link, the maximum limits for the steady-state current components i_d and i_q can be related as follows [5],

ignoring resistance effects:

$$v_d = -X_q i_q \quad (1)$$

$$v_q = X_d i_d + \omega_e \lambda_f \quad (2)$$

$$V_o^2 = v_d^2 + v_q^2 \quad (3)$$

so that

$$\left[\frac{V_o}{X_q} \right]^2 = i_q^2 + \left[\frac{X_d}{X_q} \right]^2 \left[i_d + \frac{\omega_e \lambda_f}{X_d} \right]^2 \quad (4)$$

where

- X_d d -axis stator reactance = $\omega_e L_{ds}$ (Ω),
 X_q q -axis stator reactance = $\omega_e L_{qs}$ (Ω),
 ω_e excitation frequency $p\omega_r$ (elec. rad/s),
 ω_r rotor angle frequency (mech. rad/s),
 p motor pole-pair number,
 V_o maximum available per-phase fundamental component, voltage (peak) = $(2/\pi)V_{dc}$, (V),
 V_{dc} source dc link inverter input voltage (V),
 λ_f per-phase magnetic flux linkage (Wb).

As shown in Fig. 3, (4) generates an ellipse in the orthogonal d - q plane for a given speed, source voltage, and set of motor parameters. Any combination of instantaneous current component values i_d and i_q generates a directed vector \vec{i}_s from the origin in this d - q plane. At a given rotor speed the current vector \vec{i}_s can reach anywhere inside or on the associated voltage limit ellipse during steady-state operation—but not outside it. Both ellipse radii scale inversely with rotor speed so that increasing the speed produces a family of progressively smaller nested ellipses, as shown in Fig. 3, indicating progressively smaller ranges for the steady-state stator current vector.

Fig. 4 shows the current vector operating ellipse for the laboratory 3-hp IPM drive at one particular speed. The figure also shows the desired trajectory traced out by the stator current command vector \vec{i}_s^* producing maximum torque-per-amp as the torque is varied over a wide range of positive and negative values [1]. As long as the \vec{i}_s^* command vector (comprising i_d^* and i_q^*) remains inside the ellipse, the current regulator gain is sufficiently high to force close correspondence between the commanded (\vec{i}_s^*) and resultant (\vec{i}_s) current vectors. However, if the commanded current vector extends outside the ellipse, the resultant current vector is forced to diverge from the commanded \vec{i}_s^* on a steady-state basis in order to remain within the ellipse boundaries. For motoring operation, the net effect is a significant drop in the developed torque below the desired value as the command vector is extended further outside the ellipse.

C. Saturated-Regulator Vector Relationships

For small-signal analysis, the onset of current regulator saturation can be modeled as a progressive drop in the regulator gain, giving rise to growing current errors [15]. However, on a large-signal basis, useful insights into the nature of this saturation are provided by examining the vector relationships of the current and voltage fundamental compo-

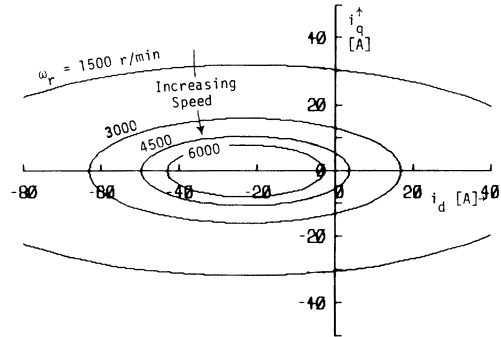


Fig. 3. Stator current vector operating range expressed as voltage-limit ellipse in rotor-referred d - q plane for several rotor speeds. Ellipses calculated using parameters of 3-hp laboratory IPM drive with $V_{dc} = 100$ V.

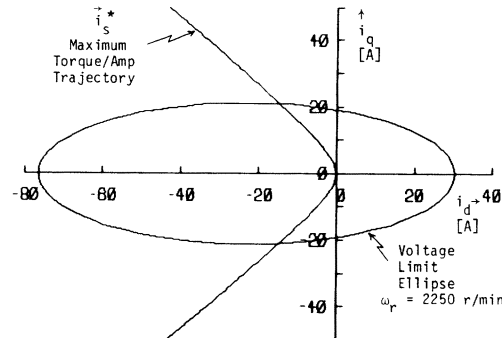


Fig. 4. Voltage-limit ellipse for fixed-speed operation superimposed on maximum torque-per-amp current command vector trajectory.

nents. Stator voltage excitation degenerates to fixed-amplitude six-step waveforms following current regulator saturation. The fundamental component of the stator voltage is represented by a vector \vec{v}_s comprising components v_d and v_q , with fixed amplitude V_o as expressed in (3) and (4). Further investigation shows that the saturated current regulator forces the orientation of \vec{v}_s to coincide with that of the difference vector $\Delta \vec{i}_s = (\vec{i}_s^* - \vec{i}_s)$, as illustrated in Fig. 5. This key relationship holds for major classes of current regulator designs, including both hysteresis and ramp-comparison configurations.

Considering the case of fixed rotor speed, one also finds that every current command vector extending outside the ellipse maps to a single steady-state operating point along the periphery of the ellipse, corresponding to six-step excitation operation (see Fig. 5). To qualify as a steady-state operating point, each resulting \vec{i}_s and \vec{v}_s vector pair must simultaneously satisfy the steady-state motor equations (1)–(4) as well as the regulator-imposed requirements described above.

The nature of this mapping is revealed by considering a sample current vector operating point along the ellipse periphery \vec{i}_{s1} (see Fig. 6), and by plotting an extended vector emanating from this vector point which parallels the associated voltage vector \vec{v}_{s1} demanded by the motor equations. One then finds that any current command vector outside the ellipse which terminates anywhere along the length of this intercept vector (such as \vec{i}_{sx} , \vec{i}_{sy}^* , and \vec{i}_{sz}^* in Fig. 6) will result in steady-state operation at the same point on the ellipse periphery at that

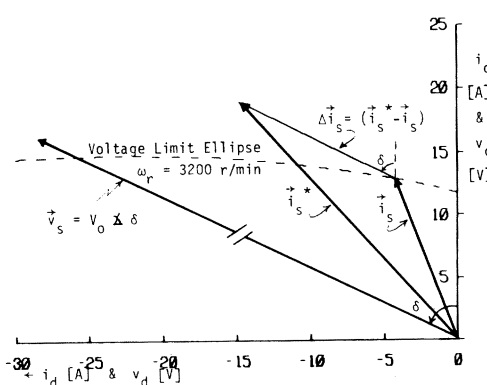


Fig. 5. Diagram illustrating constraint imposed by saturated current regulator forcing fixed-amplitude motor voltage vector \vec{v}_s into alignment with current difference vector $\Delta \vec{i}_s$.

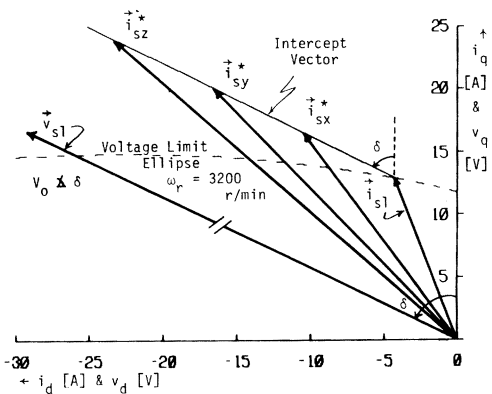


Fig. 6. Diagram illustrating equivalence of current command vectors (\vec{i}_{sx}^* , \vec{i}_{sy}^* , \vec{i}_{sz}^*) terminating on same intercept vector outside ellipse, forcing operation at saturated-regulator operating point $(\vec{i}_{s1}, \vec{v}_{s1})$.

speed, \vec{i}_{s1} . Furthermore, each such operating point corresponds to a defined average torque production.

By plotting a family of these intercept vectors generated for several points on the ellipse, as shown in Fig. 7, a macroscopic view is developed of the mapping from command to resultant current vectors during saturated-regulator operation at a fixed positive (counterclockwise) speed. The intercept vectors are also labeled with the torque of the associated operating points to illustrate the torque profile along the ellipse periphery.

In addition, the maximum torque-per-amp command trajectory has been superimposed on top of the intercept vector families of Fig. 7. The resulting intercept patterns indicate that current regulator saturation during motoring operation in the second quadrant causes the current vector \vec{i}_s to swing back along the ellipse towards the positive q -axis. This motion is accompanied by degraded torque production. Results from digital computer simulation of the laboratory IPM drive system (described later in Section IV-A) clearly illustrate these saturation characteristics in Fig. 8 for a ramp in the motoring torque command from zero. The instantaneous stator current vector (including all PWM and harmonic effects) initially follows the maximum torque-per-amp trajectory inside the ellipse (Fig. 8(a)). However, on approaching the ellipse for higher commands, the current vector swings back along the ellipse, as expected, causing the developed torque to plateau and eventually fall (Fig. 8(b)).

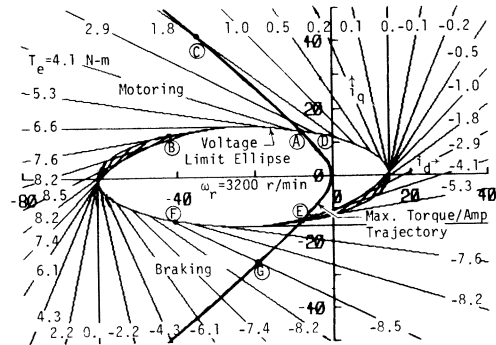


Fig. 7. Voltage-limit ellipse at fixed rotor speed with family of intercept vectors for saturated-regulator operation, superimposed on maximum torque-per-amp current command vector trajectory.

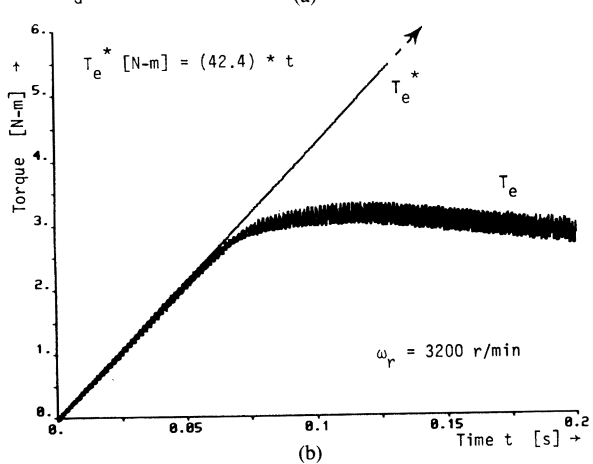
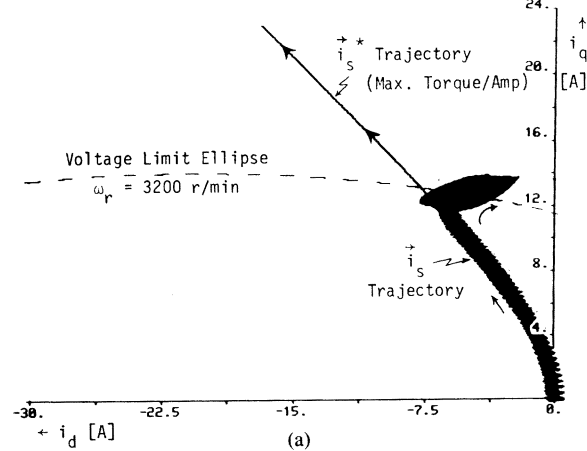


Fig. 8. (a) Simulation results showing trajectories of instantaneous command and resultant current vectors in response to torque command ramp from zero without flux weakening. (b) Simulation results for torque command ramp and developed motor torque, illustrating effects of current regulator saturation for $T_e^* > 3$ N·m.

D. Basis for Flux-Weakening Operation

An examination of the second quadrant in Fig. 7, corresponding to motoring operation for positive (counterclockwise) rotation, suggests an approach for overcoming the problems caused by current regulator saturation. Specifically, one finds that the motoring torque can be increased significantly beyond that available at the onset of current saturation at point A in Fig. 7 by forcing the operating point to move along the ellipse towards B rather than letting it drift clockwise towards D, as in Fig. 8(a). In fact, the torque continues to increase until the maximum torque point is reached at point B.

This motion of the current vector operating point from A towards B along the ellipse corresponds to increasing negative values of i_d , producing d -axis flux linkage ($= L_d i_d$) which offsets the magnet flux λ_f oriented along the positive d -axis. This generation of offsetting flux is the basis for the term "flux weakening". The IPM motor is distinguished from its SPM counterpart in that this negative d -axis current component contributes to the motor torque (in the form of reluctance torque [1]) in addition to reducing the d -axis airgap flux. However, special control means are required to force the flux-weakening motion from A towards B in the second quadrant of Fig. 7, as described in the following section.

Unlike motoring operation in the second quadrant of Fig. 7, flux weakening occurs naturally during regenerative braking in the third quadrant following current regulator saturation at point E. That is, the combination of motor- and regulator-imposed constraints causes the current vector operating point to move along the ellipse for a given speed from E towards F as the current command vector moves from E to G. The orientations of the intercept vectors in the third quadrant of Fig. 7 dictate this result, which has been confirmed by simulation and experiment. This flux-weakening action results in monotonically increasing braking torque until the maximum braking torque point is reached at F.

III. IPM FLUX-WEAKENING CONTROL ALGORITHM

A. Algorithm Description

The flux-weakening control algorithm described here was developed as a modification of the basic feedforward torque control configuration [1] briefly reviewed in Section II-B. Since one of the attractive features of the feedforward torque control algorithm (Fig. 2) is its simplicity, a goal during development of the flux-weakening extensions has been to preserve as much of this simplicity as possible. In keeping with this goal, a ground rule for this development has been that no additional feedback signals should be required beyond the phase currents and rotor position feedback already available in Fig. 2.

The key to the new flux-weakening control algorithm is the use of current feedback to identify the onset of current regulator saturation. More specifically, the buildup of error between the d -axis current command i_d^* and the resultant value i_d provides valuable detection feedback. This error is normally very small when the current regulators are not saturated because the regulator gains are set quite high. The significance of this current error can be observed in Fig. 8(a) following regulator saturation where the resulting i_d magnitude decreases as the operating point moves along the ellipse back towards the q -axis, whereas the magnitude of i_d^* continues to increase with the torque command. This current error serves as the control input for the new flux-weakening algorithm, and is designated as $\Delta i_d = i_d^* - i_{dm}$, where i_{dm} is the measured d -axis current. The measured i_{dm} can be calculated from the instantaneous phase current measurements and the rotor angle feedback:

$$i_{dm} = \frac{2}{3} \left[i_A \cos(\theta_e) + i_B \cos\left(\theta_e - \frac{2\pi}{3}\right) + i_C \cos\left(\theta_e + \frac{2\pi}{3}\right) \right] \quad (5)$$

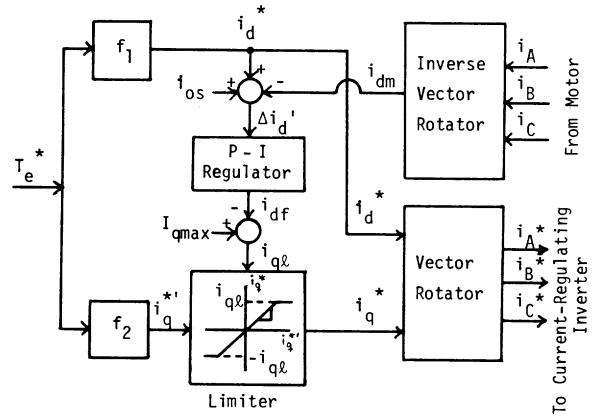


Fig. 9. Diagram of modified IPM motor drive control including new flux-weakening control feature.

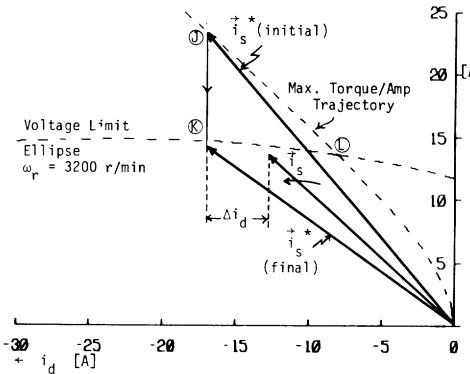


Fig. 10. Diagram illustrating action of flux-weakening control to depress i_q^* in response to Δi_d error following current regulator saturation.

where

$$\theta_e \text{ rotor angle} = p\theta_r \text{ (elec. rad)}$$

$$\theta_r \text{ rotor angle measured to phase A axis (mech. rad).}$$

A block diagram of the new proposed flux-weakening control algorithm is shown in Fig. 9. Blocks f_1 , f_2 , and the vector rotator are elements in the original feedforward torque control presented earlier in Fig. 2. The principal new control elements in Fig. 9 are the inverse vector rotator to calculate i_{dm} , a proportional-integral (P-I) regulator block, and an adjustable limiter on the q -axis current command line (i_q^*).

The basic action of the flux-weakening algorithm in Fig. 9 is to depress the q -axis current command i_q^* in response to the presence of a growing d -axis current error Δi_d , signifying current regulator saturation. By depressing i_q^* , the current command vector \vec{i}_s^* which initially lies outside the voltage-limit ellipse at a given speed (point J in Fig. 10) is forced back down inside the ellipse (to point K). As a result, the current regulators are able to regain at least partial authority to move the current vector \vec{i}_s from L towards K in Fig. 10, forcing correspondence between the commanded and resultant current vectors. The d -axis current error Δi_d is driven towards zero in the process, illustrating the negative-feedback nature of the control.

Simulation results in Fig. 11(a) demonstrate that the new flux-weakening algorithm forces the current vector to move along the outer edge of the voltage-limit ellipse as desired. In

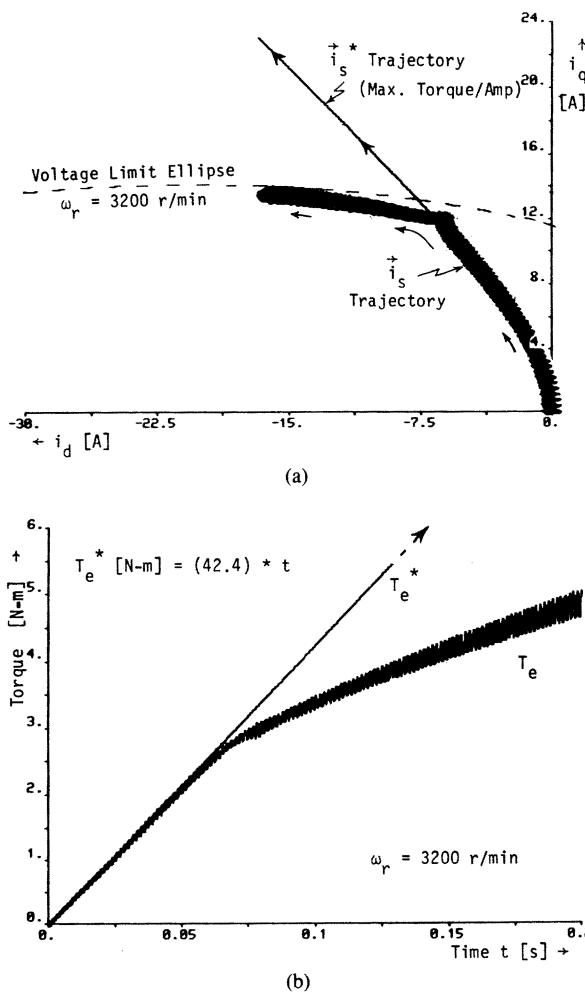


Fig. 11. (a) Simulation results illustrating flux-weakening motion of \vec{i}_s current vector initiated by new control algorithm in response to torque command ramp. (b) Simulation results showing increased torque production delivered by flux-weakening action in response to torque command ramp from zero.

contrast to the comparable results without flux weakening in Fig. 8(b), the torque in Fig. 11(b) increases monotonically (albeit at a lower ramp rate than for T_e^*) following initiation of flux weakening.

The q -axis current command limiter in Fig. 9 functions so that the output of the f_2 block, i_q^* (corresponding to the maximum torque-per-amp trajectory command), is passed through the limiter undisturbed as long as the magnitude of i_q^* is less than the adjustable limit input i_{q1} . This feature provides the desired decoupling of the flux-weakening mode operation from normal regulated-current-mode operation under all speed and load conditions until the regulator saturation transition zone is reached. Values of $I_{q\max}$ and i_{os} are adjusted to insure that the control provides adequate decoupling of the current-regulated and flux-weakening modes while delivering good transient response during mode transitions, as demonstrated in the following section.

B. Dynamic Performance of Flux-Weakening Algorithm

As described in [1], the dynamic response of the basic feedforward torque control algorithm during current-regulated

operation is very fast, limited by the response characteristics of the current regulator loops. In comparison, the dynamic response of the drive during flux-weakening operation depends on the d -axis current feedback loop, shown in Fig. 9, in combination with the saturating current regulators in their transition zones. The nonlinear nature of this closed-loop system during flux-weakening operation makes it impossible to explore the detailed dynamic response issues within the scope of this paper. Nevertheless, some observations concerning dynamic response characteristics will be provided.

Simulation results combined with empirical observations from the prototype IPM drive system indicate that the dynamic performance is quite satisfactory during flux-weakening operation. The system demonstrates well-behaved damped responses to large-signal step commands for a considerable range of P-I controller gain values (see Fig. 9), even when these steps require complete transitions of the current regulators into or out of their saturated states.

An example of this large-signal dynamic behavior is provided in Fig. 12(a), showing simulation results for two consecutive large step commands applied to the laboratory 3-hp IPM drive system at 3500 r/min. The first of these (at $t = 0.02$ s) is a large positive torque command step requiring transition into flux weakening, whereas the second large command step (at $t = 0.04$ s) pulls the system back inside the regulated-current regime. The transient response of the instantaneous torque when transitioning into flux weakening is well behaved and quite fast with a time constant of approximately 3 ms. The torque response for the subsequent transition out of flux weakening is even faster as the current regulators are released from saturation.

Further insights into the dynamic characteristics for this same transient event are provided by the instantaneous current vector \vec{i}_s trajectory in Fig. 12(b), together with the trajectory of the current command vector \vec{i}_s^* . Initially the commanded and resultant current vectors reside inside the prevailing ellipse at 3500 r/min along the programmed maximum torque-per-amp trajectory shown in the figure. Following the large positive torque command step at $t = 0.02$ s, the current command vector initially moves outside the ellipse, with i_q^* reaching the indicated $I_{q\max}$ limit. The P-I compensator in Fig. 9 immediately responds to depress the i_q^* level, pulling the command vector back towards the ellipse perimeter as indicated in Fig. 12(b). The current regulators regain their authority and initiate flux weakening by pulling the operating point vector off the initial trajectory to higher values of negative d -axis current. Subsequent reduction in the torque command at $t = 0.04$ s draws both the commanded and resultant current vectors back inside the voltage-limit ellipse, terminating flux-weakening operation.

C. Algorithm Speed Range

The upper speed limit for good performance with the Fig. 9 flux-weakening algorithm occurs in the vicinity of the IPM motor overexcitation threshold speed (i.e., the speed at which the magnet-generated back-EMF phase voltage $\omega_e \lambda_f$ equals the maximum available phase voltage $V_o = 2V_{dc}/\pi$). To understand the nature of this limit, note that, unlike the surface PM

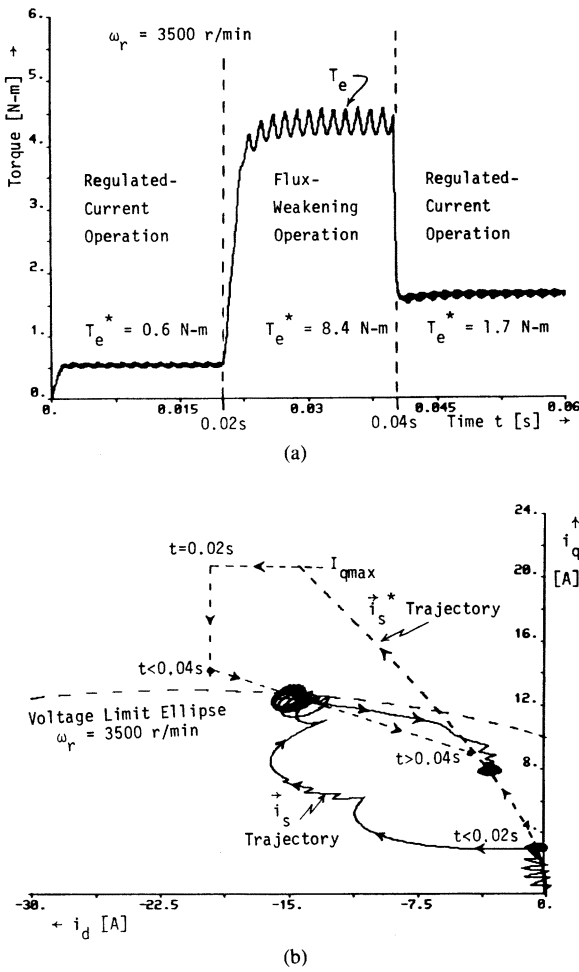


Fig. 12. (a) Simulation results illustrating transient response of instantaneous motor torque including transitions into (at $t = 0.02 \text{ s}$) and out of (at $t = 0.04 \text{ s}$) flux-weakening operation. Excitation harmonics are responsible for residual pulsating torque during flux-weakening operation. (b) Simulated trajectories for instantaneous command and resultant current vectors accompanying torque command steps in (a), illustrating control action to force flux-weakening operation during time interval $0.02 \text{ s} < t < 0.04 \text{ s}$.

motor [2], the IPM synchronous motor drive transitions into flux-weakening operation while it is still in the underexcitation speed regime ($\omega_e \lambda_f < V_o$). This is a desirable feature, since allowing the motor back-EMF to exceed the dc source voltage can cause special problems, such as dc link voltage/current surges when inverter switch gating is unexpectedly removed at high speeds.

When the IPM motor speed exceeds the overexcitation threshold, the voltage-limit ellipse representing the current vector operating locus (Fig. 3) contracts to the extent that it excludes the origin. Stator current flows at all times in this speed regime, including the zero torque point. These changes combine to compromise the performance of the Fig. 9 control algorithm during overexcitation conditions. For the laboratory IPM drive described in the following section, this feature bound the useful flux-weakening speed zone between 2300 and 5500 r/min, a 2.4:1 speed range considered typical for this class of IPM motor design with the Fig. 9 control algorithm. Although the IPM motor itself is capable of supporting wider ranges of flux-weakening operation, and alternative control

algorithm is necessary to cope with the high-speed overexcitation regime.

IV. EMPIRICAL VERIFICATION

A. Laboratory IPM Drive Description

A breadboard 3-hp IPM synchronous motor drive system has been assembled in the laboratory to explore the saturated-regulator operating characteristics of the IPM drive and to verify the new flux-weakening control algorithm described in the preceding section. A prototype four-pole ferrite-magnet IPM motor having a rotor geometry similar to that illustrated in Fig. 1(a) serves as the heart of this test drive system. Electrical equivalent circuit parameters for this machine are summarized in the Appendix. The ratio of the stator q -axis inductance L_q to the d -axis value L_d is roughly 2.5, which is typical for this class of IPM machine construction [16].

This IPM test motor has been outfitted with an encoder to provide rotor position feedback, and a bipolar-transistor PWM inverter is used to excite the motor from a 100-Vdc source. Hall-effect current sensors provide phase current feedback to close the phase current regulation loops using a PWM ramp-comparison algorithm [14]. By purposely lowering the dc link voltage to 100 Vdc, the threshold speed for current regulator saturation was forced down on 2300 r/min at 6.2 N·m shaft torque, corresponding to a delivered power of 1.5 kW at this corner transition point. Drive control electronics have been installed to implement the basic IPM feedforward torque control shown in Fig. 2, as well as the new flux-weakening algorithm presented above.

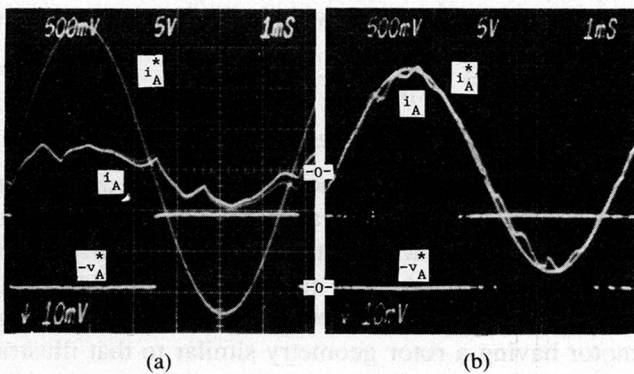
B. IPM Drive Test Results

Since the flux-weakening algorithm presented in Fig. 9 incorporates the basic feedforward torque control of Fig. 2 as a separable module, it was possible to design the drive control logic so that the flux-weakening portion can be activated at will by simply closing a switch. Tests were run over a wide range of operating conditions with the flux-weakening algorithm alternately active and inactive to investigate its operation and effectiveness.

Fig. 13 provides oscilloscopes of the commanded and resultant phase current waveforms taken for the same operating point speed and torque command with and without flux weakening. A comparison of the measured phase current waveforms clearly demonstrates the action of the flux-weakening control to pull the operating point back inside the voltage-limit ellipse at 4500 r/min, reactivating the saturated current regulators. This action results in a significant 3:1 increase in the torque production—from 1.24 N·m without flux weakening to 3.68 N·m with the algorithm activated.

Measurements of the developed torque as a function of the command level with and without flux weakening at a fixed speed of 3200 r/min are plotted in Fig. 14. These curves illustrate the elevated torque made available by flux weakening, and they agree well with the simulation results in Figs. 8(b) and 11(b).

Steady-state performance measurements taken over a range of speeds are plotted in Fig. 15, demonstrating that the flux-weakening algorithm considerably expands the IPM drive



(a)

(b)

Fig. 13. Oscilloscograms comparing operation of laboratory IPM drive at same command point and speed (4500 r/min). (a) Without flux-weakening control ($T_e = 1.24 \text{ N}\cdot\text{m}$). (b) With flux-weakening control ($T_e = 3.68 \text{ N}\cdot\text{m}$). Upper: $i_A^* = 10 \text{ A}/\text{div}$; $i_A = 10 \text{ A}/\text{div}$. Lower: $-v_A^* = 5 \text{ V}/\text{div}$ (inverted terminal V command). Horiz: $t = 1 \text{ ms}/\text{div}$.

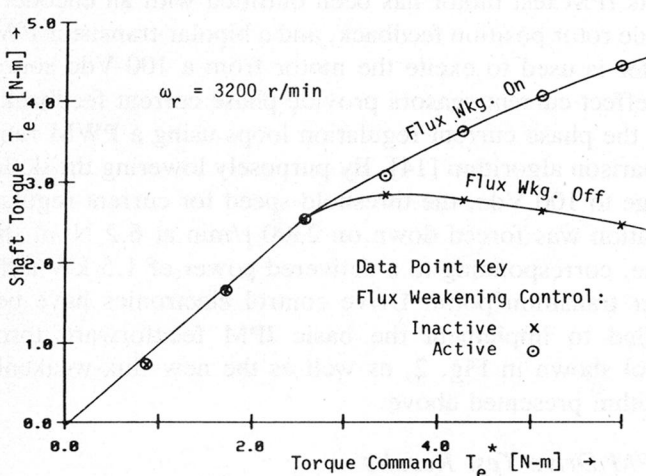


Fig. 14. Measured IPM motor shaft torque versus torque command at fixed speed, with and without flux-weakening control.

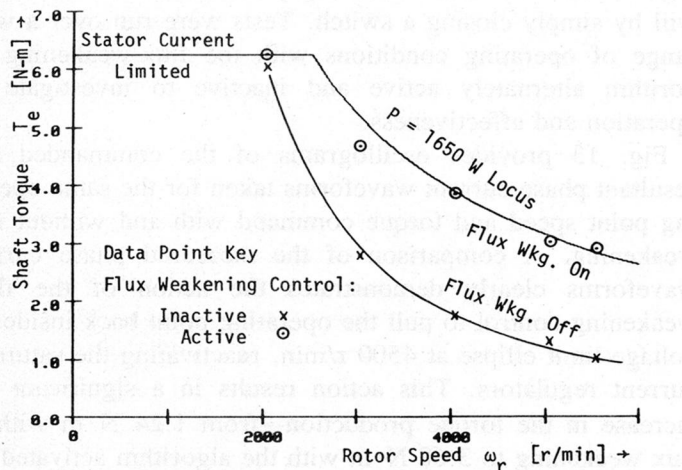


Fig. 15. Measured torque-speed operating envelope for laboratory IPM motor drive demonstrating expanded envelope with flux-weakening control activated.

operating envelope. Without flux weakening, the current regulators saturate prematurely so that the maximum available torque falls off significantly faster than $1/\omega_r$. Flux weakening expands the operating envelope of the drive out to the constant-power locus (1.65 kW for this case) at the upper end

of the speed range with no increase in the peak motor phase current beyond its peak value at the corner point speed.

V. CONCLUSION

The attractiveness of the interior PM synchronous motor for adjustable-speed applications is enhanced by its demonstrated compatibility with constant-power operation at high speeds. Key results of this investigation are summarized as follows.

- 1) The basic current-regulated feedforward torque control algorithm presented previously in [1] (see Fig. 2) cannot provide a natural transition into flux weakening during motoring operation.
- 2) Vector-graphic techniques have demonstrated how the regulator- and motor-imposed constraints combine to resist flux weakening, forcing undesired drops in the motoring torque following current regulator saturation in the absence of flux-weakening control.
- 3) A new flux-weakening control algorithm has been introduced as a modification of the current-regulated feedforward torque control algorithm to extend operation into the constant-power flux-weakening regime. The new flux-weakening control algorithm is capable of adjusting naturally to changes in the drive operating conditions, including significant variations in the dc source voltage, motor loading, and rotor speed.
- 4) The ability of this new flux-weakening algorithm to expand the drive torque-speed operating range out to the desired constant-power envelope has been verified using empirical results from a 3-hp laboratory IPM motor drive.

Finally, note that the usefulness of the flux-weakening regime operation in IPM synchronous motor drives exceeds the limits of the specific control algorithm proposed in this paper. Future demonstrations of enhanced algorithms will only further highlight the attractiveness of the IPM synchronous motor for a wide range of traction, spindle drive, and other special applications demanding high-performance constant-power operation.

APPENDIX

Per-phase equivalent circuit [1] parameter values for the prototype 3-hp four-pole ferrite-magnet IPM synchronous motor used in this investigation are listed here:

$$L_{ds} = L_{1d} + L_{md} = 2.53 \text{ mH}$$

$$L_{qs} = L_{1q} + L_{mq} = 6.38 \text{ mH}$$

$$\lambda_f = L_{md} I_f = 0.0581 \text{ Wb.}$$

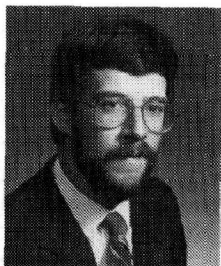
REFERENCES

- [1] T. M. Jahns, G. B. Kliman, and T. W. Neumann, "Interior permanent magnet synchronous motors for adjustable-speed drives," *IEEE Trans. Ind. Appl.*, vol. IA-22, pp. 738-747, July/Aug. 1986.
- [2] T. M. Jahns, "Torque production in PM synchronous motor drives with rectangular current excitation," *IEEE Trans. Ind. Appl.*, vol. IA-20, pp. 803-813, July/Aug. 1984.
- [3] F. Strauss, "Synchronous machines with rotating permanent-magnet fields," *AIEE Trans.*, vol. 71, pt. III, pp. 887-893, Oct. 1952.
- [4] V. B. Honsinger, "The fields and parameters of interior type ac

- permanent magnet machines," *IEEE Trans. Power. App., Syst.*, vol. PAS-101, pp. 867-875, April 1982.
- [5] B. J. Chalmers, S. A. Hamed, and G. D. Baines, "Parameters and performance of a high-field permanent-magnet synchronous motor for variable-frequency operation," *IEE Proc.*, vol. 132, pt. B, May 1985, pp. 117-124.
- [6] W. Volkrodt, "Machines of medium-high rating with a ferrite-magnet field," *Siemens Rev.*, vol. 43, pp. 248-254, 1976.
- [7] M. Lajoie-Mazenc *et al.*, "An electrical machine with electronic commutation using high energy ferrite," *Proc. IEE Small Electrical Machines Conf.*, 1976, pp. 31-34.
- [8] M. Lajoie-Mazenc, C. Villanueva, and J. Hector, "Study and implementation of hysteresis controlled inverter on a PM synchronous machine," *IEEE Trans. Ind. Appl.*, vol. IA-21, pp. 408-413, Mar./Apr. 1985.
- [9] B. Sneyers, G. Maggetto, and J. L. Van Eck, "Inverter fed PM synchronous motor for road electric traction," *Proc. Int. Conf. Electrical Machines*, 1982, pp. 550-553.
- [10] R. H. Park, "Two-reaction theory of synchronous machines: Part II," *Trans. AIEE*, vol. 52, pp. 352-355, June 1933.
- [11] B. Sneyers, D. W. Novotny, and T. A. Lipo, "Field weakening in buried permanent magnet ac motor drives," *IEEE Trans. Ind. Appl.*, vol. IA-21, pp. 398-407, Mar./Apr. 1985.
- [12] A. Consoli and A. Abela, "Transient performance of permanent magnet ac motor drives," *Conf. Rec. 1984 19th Ann. Meet. IEEE-IAS*, Chicago, IL, pp. 458-463.
- [13] E. Richter and T. W. Neumann, "Saturation effects in salient pole synchronous motors with permanent magnet excitation," *Proc. Int. Conf. Electrical Machines*, Lausanne, 1984, pp. 603-612.
- [14] D. M. Brod and D. W. Novotny, "Current control of VSI-PWM

inverters," *IEEE Trans. Ind. Appl.*, vol. IA-21, pp. 562-570, May/June 1985.

- [15] T. M. Rowan, R. J. Kerkman, and T. A. Lipo, "Operation of naturally sampled current regulators in the transition region," *Conf. Rec. 1986 21st Annu. Meet. IEEE-IAS*, Denver, CO, pp. 91-98.
- [16] M. Lajoie-Mazenc, P. Mathieu, and B. Davat, "Utilisation des aimants permanents dans les machines a commutation electronique," *RGE*, pp. 605-612, Oct. 1984.



Thomas M. Jahns (S'72-M'78) received the S.B. and S.M. degrees in 1974 and the Ph.D. degree in 1978 from the Massachusetts Institute of Technology, Cambridge, MA, all in electrical engineering.

Following a year's employment with Alexander Kusko, Inc., Needham Heights, MA, as a power engineering consultant, he joined Gould Laboratories, Rolling Meadows, IL, in 1979. At Gould he worked to develop new ac drive systems for both land and marine propulsion applications, as well as leading development projects in high-performance ac drives for industrial applications. He joined General Electric Corporate Research and Development in 1983, where he has pursued new ac drives technology in the Power Electronics Laboratory. His technical efforts have included development of high-performance PM servo drives for aircraft actuator and accessory applications. In 1986 he became Manager of the Power Electronics Control Program.

Dr. Jahns in serving as an officer of the Industrial Drives Committee and is the recipient of four IEEE-IAS Prize Paper Awards.